

1 **The hydro-mechanical interaction in novel polyurethane-bound pervious** 2 **pavement by considering the saturation states in the unbound granular** 3 **base course**

4 **Abstract.**

5 Based on the recent development of novel polyurethane-bound pervious mixtures (PUPM),
6 the widespread application of fully permeable pavement (FPP) structures has become viable,
7 which entails significant environmental benefits for the transport infrastructure. However, the
8 saturation state has a major influence on the performance and durability of FPP, especially on
9 the UGB material. The build-up and dissipation of pore-water pressure generated by intermit-
10 tent dynamic vehicle loading is recognized as a critical factor influencing the bearing capacity
11 of UGB layer. The majority of research on the FPP has focused on phenomenological ap-
12 proaches, while the underlying mechanisms of hydro-mechanical interaction in UGB layer and
13 the influence on FPP structure are still mostly unclear. This study aims to characterize the
14 changes in dynamic response in FPP under various saturation conditions by considering the
15 hydro-mechanical interaction within UGB layer. To achieve this objective, a full-scale test
16 track with a PUPM wearing course was designed and constructed. Pressures and water distri-
17 bution were characterized from embedded sensors within different layers of test track when
18 subjected to the accelerating pavement test (APT). Additionally, based on the coupled stress-
19 dependent moisture-sensitive cross-anisotropic elastic (SMAE) model, the water distribution
20 within FPP structure and the dynamic response of UGB in the rainfall events were both char-
21 acterized and solved by finite element modeling (FEM). The results predicted by the proposed
22 SAME model correspond to the field measurements. Based on the developed SAME model,
23 the distribution of water in the whole pavement structure was evaluated; also, the influence of
24 the water content on the resilient modulus distribution within the UGB layer was analyzed.
25 Based on the predictions for the stress state of the UGB layer, sensitive analysis based on sur-
26 face thickness was proposed.

- 1 **Keywords:** Water content, Matric suction, Unsaturated flow, Hydro-mechanical interaction,
- 2 Polyurethane bound pervious material (PUPM).

1 **1 Introduction**

2 To recover the natural hydrological cycle and restore the resilience regarding the risk of
3 urban flooding, fully permeable pavements (FPP) are implemented by directly allowing the
4 rainwater to seep through the pavement surface into the subgrade. This consequently relieves
5 the urban drainage system and supports the natural hydrological cycle (Li, H. et al. 2012, Sun,
6 W. et al. 2018).

7 Apart from the high hydraulic conductivity, the porous pavement can also make contribu-
8 tions to the noise absorption in the transportation system (Ding, Y. and Wang, H. 2019, Cao, R.
9 et al. 2020). However, with a lower content of fine aggregate, the weak resistance of the pore
10 structure to shear-stress leads to high susceptibility to grain raveling (Mo, L. et al. 2009, Zhang,
11 Y. and Leng, Z. 2017). Adhesion failure and short lifespans of porous mixtures have been the
12 main challenge, restricting the widespread application of FPP. The presented innovative poly-
13 urethane (PU) bound permeable material was developed to gain highly favorable mechanical
14 properties. The PU bound pervious material (PUPM) shows that the combination of high func-
15 tionality and favorable mechanical properties can be achieved by replacing conventional bind-
16 ers with PU. High resistance to deformation and fatigue of PUPM were also observed in later
17 lab-research, which made it possible to promote the large-scale application of FPP (Lu, G. et
18 al. 2019a, Lu, G. et al. 2019b).

19 However, in the actual service environment, the porous pavement structures are mostly in
20 the unsaturated state with the filtration and the upward movement of moisture in sublayers and
21 soil, where multi-physical processes occur, such as freezing and spalling, drying and shrinkage,
22 hydro diffusion and subsidence, capillarity and cracking (Wang, C.Y. and Cheng, P. 1997, Kha-
23 lili, N. et al. 2014). Each one of these processes can result in complex effects which will lead
24 to significant influences on the pavement behavior. (Khalili, N. et al. 2004, Kettil, P. 2005).
25 The underlying mechanisms of the hydro-mechanical interaction between pore-water and the
26 solid skeleton, which dictates the structural behavior of FPP remain unknown.

1 FPP system including permeable surface, unbounded granular base (UGB) layer and subsoil
2 must function under the stress of both water and traffic loading. Due to the high porosity and
3 permeability of the pervious surface, water can quickly infiltrate through the surface layer and
4 accumulate in the UGB layer. In which case, the UGB layer is more sensitive to moisture,
5 which is one of the serious problems affecting the performance of the whole FPP structure (Gu,
6 F. et al. 2014, Gu, F. et al. 2018).

7 Based on preliminary research, the failure on the fully permeable pavement (FPP) con-
8 structed with a PUPM surface is mainly caused by the failure in the unbound granular material
9 (UGB) in the substructure, which provides the foundational support to the surface layer and
10 distributes the stresses (Lu, G. et al. 2020). In addition, a large number of studies have shown
11 that the UGB layer behavior is highly nonlinear and anisotropic, which makes the UGB layer
12 more complicated in the case of permeable pavement structures. In particular, hydro-mechani-
13 cal interaction can significantly change the modulus of UGB, which in turn affect the service
14 life of FPP, and results in completely different mechanical distributions in the pavement layers.
15 Hence, a good understanding of the corresponding constitutive behavior of the UGB under the
16 influence of moisture is vital for the design of permeable pavements and the analysis of the
17 mechanical response. Recently, several successful constitutive models have been established
18 for UGB based on the cross-anisotropic and nonlinear behavior (Zhang, Y. et al. 2018, Gu, F.
19 et al. 2018). Simulations which included the meso-scale mechanism of anisotropy in granular
20 materials corresponded very well with the laboratory test results (Zhang, J. et al. 2018, Gu, F.
21 et al. 2014). However, due to the lack of systematical, large scale experimental investigation of
22 the mechanical and hydraulic properties in the pavement, the coupled models remain to be fully
23 validated.

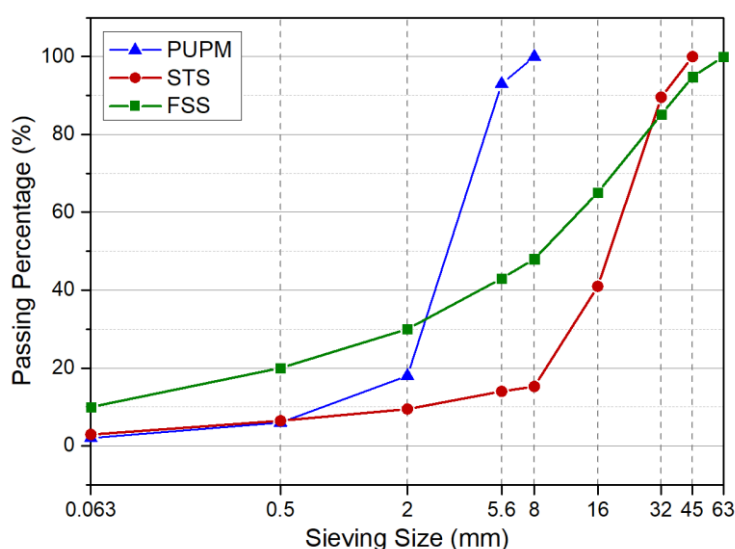
24 To further investigate the vehicle loading response of FPP with the novel PUPM, a full-scale
25 test track was constructed with a series of embedded sensors including total pressure sensors,
26 pore pressure sensors and water content meters. With the aid of accelerating the pavement test

1 (APT), the dynamic responses of the permeable pavement were studied. The water distribution
 2 mechanism in the FPP structure during a rainfall event was characterized by the unsaturated
 3 flow model. Additionally, based on the modified hydro-mechanical model, FEM simulations
 4 were conducted under different saturation states. The basic recommendation of optimizing FPP
 5 structural design under heavy traffic loading has been eventually suggested.

6 **2 Materials and experimental setup**

7 **2.1 Materials and test track**

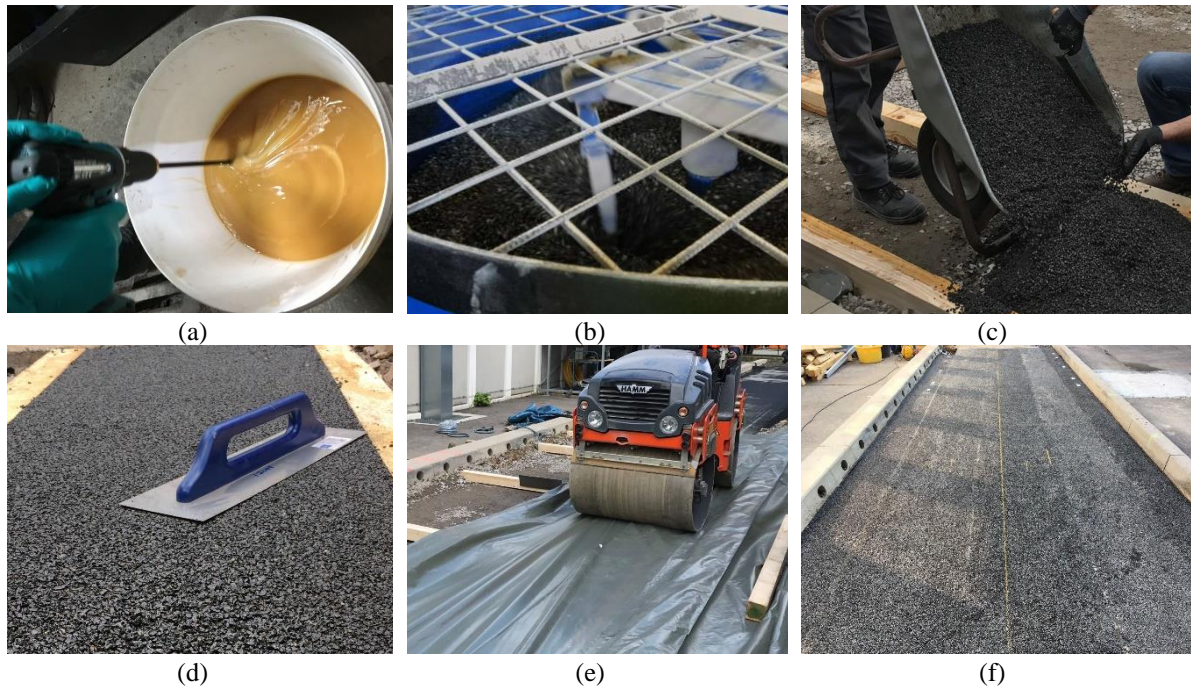
8 Previous studies have demonstrated the excellent performance of polyurethane bound per-
 9 vious mixtures (PUPM) with respect to its mechanical and functional performance compared
 10 to conventional porous asphalt mixtures (Lu, G. et al. 2019a). In the present research, PUPM
 11 was selected as the permeable surface material. Unbound granular materials, Schottertrag-
 12 schicht (STS) 0/45mm and Frostschutzschicht (FSS) 0/63mm, were utilized for constructing
 13 the UGB and subgrade layer of the test track respectively. The gradations of the materials ap-
 14 plied in the test track are given in Figure 1.



15 Figure 1. Gradation of materials used in the test track

16 The two-component polyurethane (PU) binder used in this study is provided by BASF Pol-
 17 yurethane GmbH. Its physical and chemical properties have been thoroughly documented in
 18

1 the previous study (Lu, G. et al. 2019a and Lu, G. et al. 2019b). The PUPM used in the labor-
 2 atory and the test track contained 6 % PU binder and achieved an air void content of 28 %; the
 3 construction process is shown in Figure 2. Before mixing with the aggregate, the two compo-
 4 nents (Polyol and Isocyanate) of the binder must be fully mixed around 2 minutes to ensure the
 5 full polymerization. The mixing process of PU binder and aggregates needs to be kept within
 6 5 minutes, and the paving and compaction process needs to be completed within 25-30 minutes.

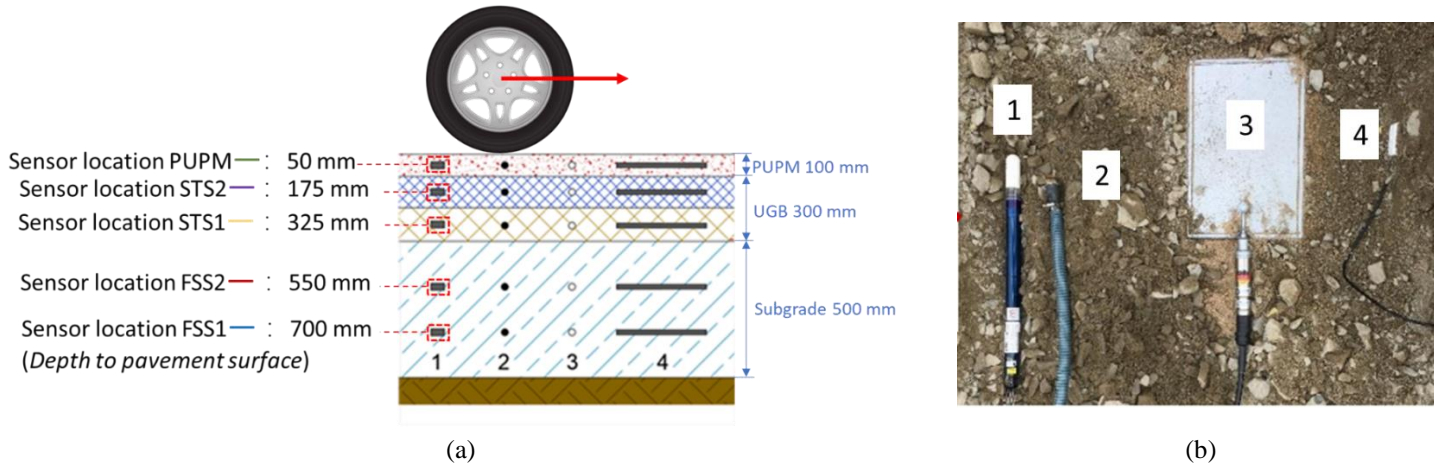


7 Figure 2. The preparation process of the PUPM pavement surface: (a) The mixing of polyure-
 8 thane binder; (b) The mixing process of aggregate and PU binder; (c), (d)and (e) The paving
 9 and compaction process of PUPM layer; (f) Paved test track;

10 2.2 The multi-physical measurement system

11 To monitor the service performance of the FPP, sensors were instrumented in all five layers,
 12 included total pressure sensor, pore-water pressure sensor, temperature sensor, and volumetric
 13 water content sensor. The location of the instruments and their technical properties are listed in
 14 Figure 3 and Table 1 respectively. All sensors were strictly controlled to be level with the road
 15 surface and exactly under the wheel loading path.

1



2





3

Figure 3 (a) The location of sensors implementation; (b) Field instrumentation (The detail of sensors 1-4 can be shown in Table 1)

4

5

Table 1 The technical data of sensors

Number	Sensor	Name	Model	Measurement Range	Accuracy
1		Tensiometer	T4	+1000 hPa to -850 hPa	± 5 hPa
2		Pore air pressure sensors	DPM 321	100 mbar to 600bar -25 °C to 85 °C	$< \pm 0.25\%$ FSO
3		Earth pressure/temperature cell	E 20/30 AU 20T Type C	0 to 20 bars -25 °C to 60 °C	$< 0.5\%$ $< 0.5\%/^{\circ}\text{C}$
4		Soil moisture sensor	GS1	0 to 57% VWC	± 0.03 m ³ /m ³

6 2.3 Accelerated pavement testing

7

8

9

10

11

12

13

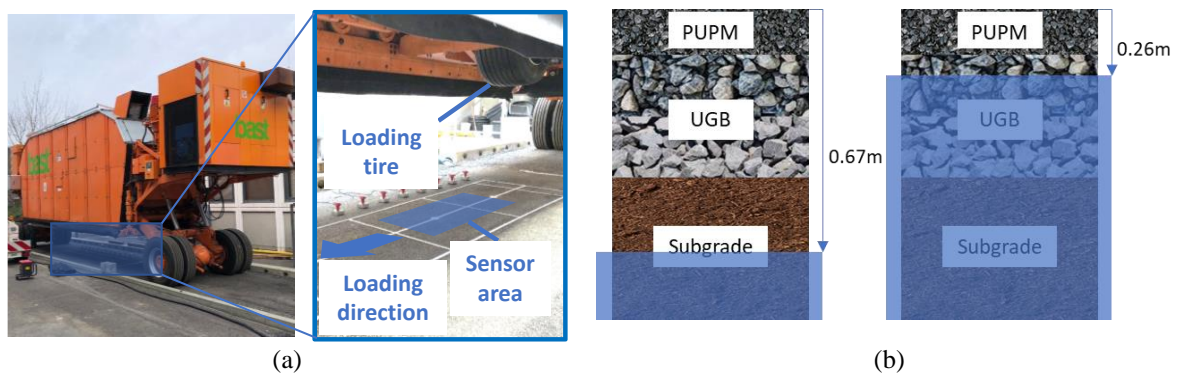
14

15

To gain a deeper understanding of the hydro-mechanical behavior of the pavement and the impacts of saturated and partially saturated conditions on the stability of the structure, an accelerated pavement testing (APT) was performed on the test track (Figure 4, a). The greatest advantage of APT is the ability to use maintain constant speeds, ensure a regular wheel path and the large number of axle load repetitions in short periods (Liu, P. et al. 2017). In collaboration with the Bundesanstalt für Straßenwesen (BASt), the Mobile Load Simulator MLS30 was operated on the test track at the RWTH Aachen University as shown in Figure 4. The MLS30 can simulate wheel loads between 40 and 75 kN through 4 bogie-mounted wheels moving in a continuous circular motion within the device (Figure 4, b). The tire pressure is set

1 to 0.85 MPa while the speed of the bogies can be varied between 7 and 22 km/h, allowing for
 2 load repetitions between 2000 and 6000 per hour. Apart from the ability to accurately study the
 3 hydro-mechanical behavior of the unbound layers and the evolution of undesirable accumu-
 4 lated pore pressure, the high loading rate of the MLS30 allows for an accurate evaluation of
 5 the expected service life. The APT test was carried out on the test track for two different satu-
 6 ration states: (a) dry or lower saturated state: no external water added into the test track with -
 7 0.67 m water level; (b) saturated state or high saturated state: the test track was fully saturated
 8 by pouring water through the pavement surface, after one day relaxing a steady water level of
 9 -0.26 m was measured). Three different velocities were used for each saturation state, namely
 10 7km/h, 14km/h and 22km/h. Each speed was set total 20.000 daily axle passages.

11



12

13 Figure 4 (a) The APT test based on MLS30; (b) A schematic diagram of FPP in two differ-
 14 ent saturation states

15 3 Theoretical background

16 3.1 Unsaturated flow model through the pervious pavement

17 In most circumstances, the permeable pavement is in a partially saturated state. The pores in
 18 the unsaturated zone are filled with water as well as air; matric suction is also active in the area.
 19 A gradient in the hydrological head leads to the flow of water. More specifically, the difference
 20 in matric potential causes water to flow towards the unsaturated area (Fredlund, D.G. et al.
 21 1993). The Richards equation has been widely adopted to analyze water flow under unsaturated
 22 conditions (Hall, C. 1977; Van Genuchten, M.T. 1980):

$$\frac{\partial \theta}{\partial t} = \frac{\partial}{\partial x} \left[K(h) \frac{\partial h}{\partial x} \right] + \frac{\partial}{\partial z} \left[K(h) \frac{\partial h}{\partial z} \right] + \frac{\partial K(h)}{\partial z} \quad \text{Eq. 1}$$

1 Where, z is the vertical coordinate along with the pavement depth [m], x is the horizontal
 2 coordinate along the wheel path [m], t = time [s], θ is the volumetric water content, K is the
 3 permeability [m/s], and h denotes the hydraulic head [m].

4 Studies on water flow in the unsaturated zones have shown that the volumetric water content,
 5 the permeability and the matric suction are interconnected (i.e., volumetric water content and
 6 hydraulic conductivity can both be formulated as a function of the matric suction) (Celia, M.A.
 7 et al. 1990; Gray, W.G. and Hassanizadeh, S.M. 1991).

8 **3.1.1 Soil Water Characteristic Curves**

9 In unsaturated porous media, the Soil Water Characteristic Curves (SWCC) describes the
 10 relationship between matric suction and saturation and plays a significant role in predicting the
 11 hydraulic as well as the mechanical properties of porous material. Empirical models to describe
 12 the water retention properties of porous material were mainly presented by Brooks and Corey
 13 (Brooks, R. and Corey, T. 1964), van Genuchten (Van Genuchten, M.T. 1980), and Fredlund
 14 and Xing (Fredlund and Xing, 1994). Based on the research conducted previously (Törzs, T. et
 15 al. 2019), the van Genuchten model for water characterization was selected in this research for
 16 the porous pavement material. In Eq. 2, α_{VG} , m_{VG} and n_{VG} are constants in the constitutive
 17 equation. For the determination of the parameter m_{VG} , the simplified approach by Mualem
 18 (Mualem, Y. 1977) was selected, see Eq. 3.

$$S_e(s) = \frac{1}{(1 + (\alpha_{VG}s)^{n_{VG}})^{m_{VG}}} \quad \text{Eq. 2}$$

$$m_{VG} = 1 - \frac{1}{n_{VG}} \quad \text{Eq. 3}$$

19 The term of effective saturation, S_e is mainly used in the present study, which was defined
 20 in terms of the actual saturation, S_r :

$$S_e = \frac{S_r - S_{r,res}}{S_{r,max} - S_{r,res}} \quad \text{Eq. 4}$$

1 Where, $S_{r,res}$ is the actual-residual saturation and $S_{r,max}$ is the actual-maximum saturation
2 under fully saturated condition.

3 **3.1.2 Models for the unsaturated hydraulic conductivity**

4 Pore structure characteristics are usually used to estimate the permeability K in porous me-
5 dia. Most existing models are based on the pore characteristics in terms of grain size distribu-
6 tion (GSD) or other measured indices. Because different pore indices regarding the pore struc-
7 ture, pore shape factor and tortuosity are very difficult to measure, this modeling approach is
8 often based on a number of assumptions; in contrast, the model based on the GSD is more
9 convenient and allows for empirical refinement. Two famous approaches for predicting the
10 permeability (K) based on the GSD are the Hazan equation and the Kozeny-Carman Model
11 (KCM). Contrary to the Hazan model based on the effective aggregate diameter, the KCM
12 considers the entire GSD, the void ratio as well as the shape factor to predict K . The accuracy
13 of the KCM was observed to surpasses that of the Hazan equation (Carrier III, W.D. 2003). As
14 a result, the KCM has become widely adopted for modelling the hydraulic conductivity in po-
15 rous materials and pavements (Oeser, M. et al. 2012). For the pervious pavement materials, the
16 modified KCM model developed in previous research (Lu, G. et al. 2020a) was adopted to
17 derive the unsaturated flow model:

$$K_{KCM}^m = \frac{\gamma_w}{\mu_w \cdot C_{k-c}} \cdot \frac{n_e}{\tau^2 S_{Ae}^2} \quad \text{Eq. 4}$$

18 Where, μ_w denotes the viscosity of water, which is approximately 1×10^{-6} KPa s at 20°C;
19 γ_w represents the unit weight of water, which is 9810 N/m³; C_{K-C} is the empirical Kozeny–
20 Carman coefficient for which a value of 5 is suggested. For the pore characteristics, n_e repre-
21 sents for effective porosity, τ denotes to tortuosity while S_{Ae} is specific surface area. Most previous
22 studies on the hydraulic conductivity of porous material are conducted for saturated flow within

1 individual fields. From the semi-empirical relationship firstly proposed by Brooks & Corey,
2 the permeability of partially saturated materials can be described as follows:

$$K_W = K_E \cdot S_e^{\left[\frac{2+3\lambda_p}{\lambda_p}\right]} \quad \text{Eq. 5}$$

3 In Eq. 5, K_E denotes to the permeability of porous media for water tested under normal la-
4 boratory testing standards and λ_p gives the value of the pore-size distribution index determined
5 as the average slope of the SWCC in this research. Similarly, the unsaturated permeability of
6 the air phase can be presented in the following equation:

$$K_A = K_E \cdot (1 - S_e)^2 \left(1 - S_e^{\left[\frac{2+3\lambda_p}{\lambda_p}\right]} \right) \quad \text{Eq. 6}$$

7 By substituting K_E with K_{KCM}^m from the KCM model, the partial permeability of both phases
8 can be directly derived from the grain size distribution. Hence, the modified unsaturated per-
9 meability model for the water and the air phase can be written as shown in Eq. 7 and Eq. 8:

$$K_W^m = K_{KCM}^m \cdot S_e^{\left[\frac{2+3\lambda_p}{\lambda_p}\right]} \quad \text{Eq. 7}$$

$$K_A^m = K_{KCM}^m \cdot (1 - S_e)^2 \left(1 - S_e^{\left[\frac{2+\lambda_p}{\lambda_p}\right]} \right) \quad \text{Eq. 8}$$

10 **3.2 The constitutive model for pervious pavement material**

11 **3.2.1 The Resilient Modulus Model for UGB**

12 The resilient modulus of unbound aggregates has been widely recognized as the primary
13 mechanical property of the base course required in the mechanistic-empirical design of pave-
14 ment structures. In order to determine the resilient modulus of unbound aggregates, various
15 models have been developed (Uzan, J. 1985).

16 Among these, the most recognized one is the generalized model as follow (Zhang, Y. et al.
17 2018):

$$E_Z = k_1 P_{atm} \left(\frac{I_1}{P_{atm}} \right)^{k_2} \left(\frac{\tau_{oct}}{P_{atm}} \right)^{k_3} \quad \text{Eq. 9}$$

where I_1 represents the first invariant of the stress tensor; τ_{oct} stands for the octahedral shear stress; P_{atm} is the atmospheric pressure; and k_1 , k_2 , and k_3 are regression coefficients.

3.2.2 Cross-anisotropy of UGB material

It has been widely researched and proven that the cross-anisotropic model of UGB should be considered in the numerical investigation of pavement performance under consideration of nonlinear material (Tutumluer, E. and Thompson, M.R., 1997, Adu-Osei, A. et al. 2001, Zhang, Y. et al. 2018). Cross-anisotropy means that material properties are different between the horizontal and vertical planes while the material properties remain the same in the horizontal plane. Eq. 10 and 11 were employed for characterizing the cross-anisotropic properties of the UGB layer in FPP systems.

$$\sigma'_{ij} = \begin{bmatrix} \sigma'_{xx} \\ \sigma'_{yy} \\ \sigma'_{zz} \\ \sigma'_{xy} \\ \sigma'_{yz} \\ \sigma'_{zx} \end{bmatrix} = \frac{E_z}{\alpha_0 \beta_0} \begin{bmatrix} n(1 - nv_{zx}^2) & n(v_{xy} - nv_{zx}^2) & nv_{zx}\alpha_0 & 0 & 0 & 0 \\ n(v_{xy} - nv_{zx}^2) & n(1 - nv_{zx}^2) & nv_{zx}\alpha_0 & 0 & 0 & 0 \\ n(1 - nv_{zy}^2) & n(1 - nv_{zy}^2) & 1 - nv_{zy}^2 & 0 & 0 & 0 \\ 0 & 0 & 0 & \frac{1}{2}n\beta_0 & 0 & 0 \\ 0 & 0 & 0 & 0 & m\alpha_0\beta_0 & 0 \\ 0 & 0 & 0 & 0 & 0 & m\alpha_0\beta_0 \end{bmatrix} \begin{bmatrix} \varepsilon_{xx} \\ \varepsilon_{yy} \\ \varepsilon_{zz} \\ 2\varepsilon_{xy} \\ 2\varepsilon_{yz} \\ 2\varepsilon_{zx} \end{bmatrix} \quad \text{Eq. 10}$$

$$n = \frac{E_x}{E_z} \quad \text{Eq. 11}$$

$$m = \frac{G_{ZX}}{E_z}$$

$$\alpha_0 = 1 + v_{xy}$$

$$\beta_0 = 1 - v_{xy} - 2nv_{zx}^2$$

Where, G_{ZX} is shear modulus in the vertical plane, E_z is the resilient modulus in the vertical plane, E_x is the resilient modulus in the horizontal plane, v_{zy} and v_{zx} represent Poisson's ratio in the vertical and horizontal planes respectively.

3.2.3 The hydro-mechanical constitutive model for pervious pavement material

Fundamentally, permeable pavements can be considered as a three-phase material containing solids, moisture and gas, especially when the pavement is in an unsaturated state. It must be addressed that, when vehicles traverse the pavement, the generation and dissipation of pore

1 pressure in the water and air phases play a critical role in the failure mechanisms of permeable
2 pavement (Alobaidi, I. and Hoare, D.J. 1996).

3 Based on this, the effective stress concept was developed to determine the strength of the
4 unsaturated materials by considering the pore pressures (Loret, B. and Khalili, N. 2002). In its
5 mathematical formulation, Terzaghi's effective stress σ' , is defined as the difference between
6 the total stress and pore-water pressures. One of the most renowned modified effective stress
7 concepts is generally attributed to the approach established by Bishop (Bishop, A.W. 1954),
8 where the effective stress can be rewritten as shown in Eq. 12, with the introduction of the
9 effective stress parameter χ , which governs the interaction between the solid and the liquid
10 phase.

$$\sigma' = \sigma - \chi s = \sigma - \chi(P_a - P_w) \quad \text{Eq. 12}$$

11 Wherein the effective stress parameter can be defined as following:

$$\chi = \begin{cases} 1 & s_e \geq s \\ \left(\frac{s_e}{s}\right)^\Omega & s_e < s \end{cases} \quad \text{Eq. 13}$$

12 Ω is determined as 0.55 in the current research based on empirical regression (Oeser, M. et
13 al. 2012). To incorporate the moisture-dependent properties of UGB's resilient modulus, a new
14 constitutive model can be derived based on the effective stress:

$$E_z^m = k_1 P_{atm} \left(\frac{I_1 - 3\chi s}{P_{atm}}\right)^{k_2} \left(\frac{\tau_{oct}}{P_{atm}}\right)^{k_3} \quad \text{Eq. 14}$$

15 By coupling Eq. 1, 9, 10 and 14, the Stress-dependent moisture-sensitive cross-anisotropic
16 elastic (SMAE) model was derived and is proposed to investigate the hydro-mechanical inter-
17 action in the permeable pavement.

18 **4 The Finite Element Modeling of FPP considering the hydro-mechanical** 19 **interaction**

20 **4.1 The development of the FEM for FPP**

21 *Weak form based FEM in COMSOL program*

1 A number of researches have modeled asphalt concrete behavior by using the weak-form
2 partial differential equation (PDE)-based FEM techniques in the COMSOL
3 MULTIPHYSICS® program (Liu, Z. and Yu, X., 2014, Zhang, Y. et al. 2015, Zhang, J. et al.
4 2018, Luo, X. et al. 2020). The weak-form PDE-FEM has been found to have advantages when
5 solving various coupling problems with interdependent variables regarding the model inputs
6 and the dependent variables. Modeling a UGB material with a SMAE modulus is a complex
7 coupling process that includes an interdependence between modulus, stress, deformation and
8 saturation. However, the interdependence can be solved by creating additional dependent var-
9 iables in the weak-form PDE FEM to define the SMAE model. Unlike using Abaqus, there is
10 no need for this method to program any material subroutine. In this study, the authors model
11 the permeable pavement based on the PDE-FEM.

12 ***Load and Boundary Conditions.***

13 The pavement structure with the APT test was modeled in COMSOL MULTIPHYSICS® as
14 shown in Figure 5. Based on the dimensions of the test track and the in-situ loading section,
15 the simulated structure was created with a length of 3500 mm. The three layers were modeled
16 with the following thickness: 100 mm PUPM surface, 300 mm UGB layer and 500 mm sub-
17 grade layer. The purpose of the experiment design was to control the water content in the entire
18 pavement structure. In the actual test, the side and bottom of the pavement were sealed by a
19 waterproof membrane. Correspondingly, in the simulation, the design rainfall event can only
20 be applied from the surface layer and is retained in the pavement structure.

21 Corresponding to the APT test, a traveling tire patch with a uniform vehicle contact stress of
22 350 kPa was applied on the PUPM surface on a 150 mm wide loading area with a maximum
23 speed of 22 km/h. The loads were simplified as uniform vertical loads. The loading speed was
24 defined with the square wave function $\text{Rect}()$ and the analytic function $\text{Pulse}(X) =$
25 $\text{Rect}(X - \text{Loadspeed} * t)$ of the applied loads and coordinate, which are already embedded in
26 the COMSOL software.

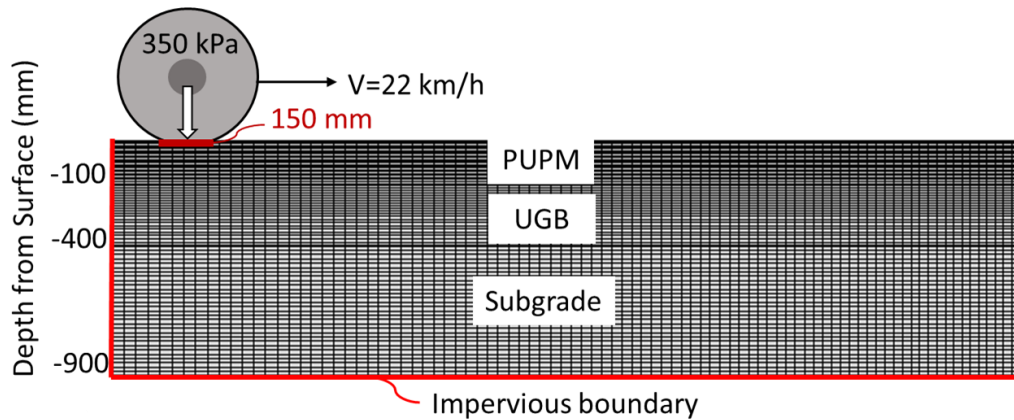


Figure 5 The FEM model of FPP based on PUPM layer

4.2 Determination of the model parameters

In the present research, the modeling of unsaturated flow included the van Genuchten prediction of SWCC, the modified KC permeability model as well as the Richard flow model for unsaturated flow. The parameters of the SWCC model were derived based on the measurements from a hanging water column apparatus in accordance with ASTM D6836-16. The saturated and unsaturated flow model, used in the current model was also validated in the previous research based on permeability results from the laboratory (Oeser, M. et al. 2012, Törzs, T. et al. 2019). Table 2 lists the key parameters of unsaturated flow modeling.

Table 2. Unsaturated flow parameters used in the finite element modeling

Materials	γ_w (N/m^3)	μ_w ($Pa \cdot s$)	$S_{r,max}$ (-)	$S_{r,res}$ (-)	α_{VG} ($1/m$)	m_{VG} (-)	n_{VG} (-)
PUPM Layer	9810	10^{-3}	0.295	0.011	4.255	0.82	5.54
UGB Layer	9810	10^{-3}	0.252	0.020	8.102	0.4	1.66
Subgrade soil layer	9810	10^{-3}	0.186	0.048	0.226	0.17	1.20

Different constitutive material models, i.e., Linear Isotropic Elastic (LIE) model, Linear Cross-anisotropic Elastic (LAE) model, Stress-dependent Cross-anisotropic Elastic (SAE) model and Stress-dependent Moisture-sensitive cross-Anisotropic Elastic (SMAE) model, were all taken into account and evaluated in finite element simulations. Table 3 lists the parameters required for these constitutive material models. The PUPM was modeled as an elastic

1 material, and its elastic modulus was obtained from the uniaxial compression test documented
 2 in the previous study (Lu, G. et al. 2019). Crushed graywacke aggregates were used to construct
 3 the UGB layer, which has a maximum dry density of $2.15 \times 10^3 \text{ kg/m}^3$ and an optimum water
 4 content of 7.3%. The non-linear and cross-anisotropic parameters of UGB material can be
 5 obtained by conducting repeated load triaxial tests at different stress levels. In the current study,
 6 the values of modeling parameters for UGB were adopted based on the previous research,
 7 which corresponds to the medium resilient modulus of the base material (Zhang, Y. et al. 2019).
 8 Based on the average vertical modulus value predicted by SAE, 110 MPa was selected as the
 9 constant vertical modulus of LAE and LIE. The subgrade was also predicted as an elastic ma-
 10 terial (with maximum dry density of $2.17 \times 10^3 \text{ kg/m}^3$ and optimum water content 7.8%).
 11 The elastic modulus of subgrade was estimated from the California bearing ratio tests (ASTM
 12 D1883-14) based on the empirical equation $E = 2.55 \times CBR^{0.64}$ according to APA 2004. The
 13 finite element modeling was then conducted using the commercial COMSOL
 14 MULTIPHYSICS® software.

15 Table 3. Material parameters used in the finite element modeling.

Materials	k_1	k_2	k_3	n	m	v_{zx}	v_{xy}
PUPM Layer	$E_1 = 3.31 \text{ GPa}; v_1 = 0.16$						
UGB-SMAE	1281	0.81	-0.08	0.45	0.35	0.38	0.43
UGB-SAE	1281	0.81	-0.08	0.45	0.35	0.38	0.43
UGB-LAE	$E_z = 110 \text{ MPa}$			0.45	0.35	0.38	0.43
UGB-LIE	$E_z = 110 \text{ MPa}$						
Subgrade soil layer	$E_3 = 69 \text{ MPa}; v_3 = 0.4$						

16 Notes: E_1 and E_3 are elastic modulus values of the PUPM layer and the natural subgrade soil
 17 layer, respectively; v_1 and v_3 represent the Poisson's ratios of the PUPM surface layer and the
 18 natural subgrade soil layer. E_z is the vertical modulus of the UGB layer. $k_1, k_2, k_3, v_{zx}, v_{xy}$ are
 19 the nonlinear and cross-anisotropic parameters of SAME, SAE and LAE, the value of which
 20 were selected based on the previous study (Zhang, Y. et al. 2019).

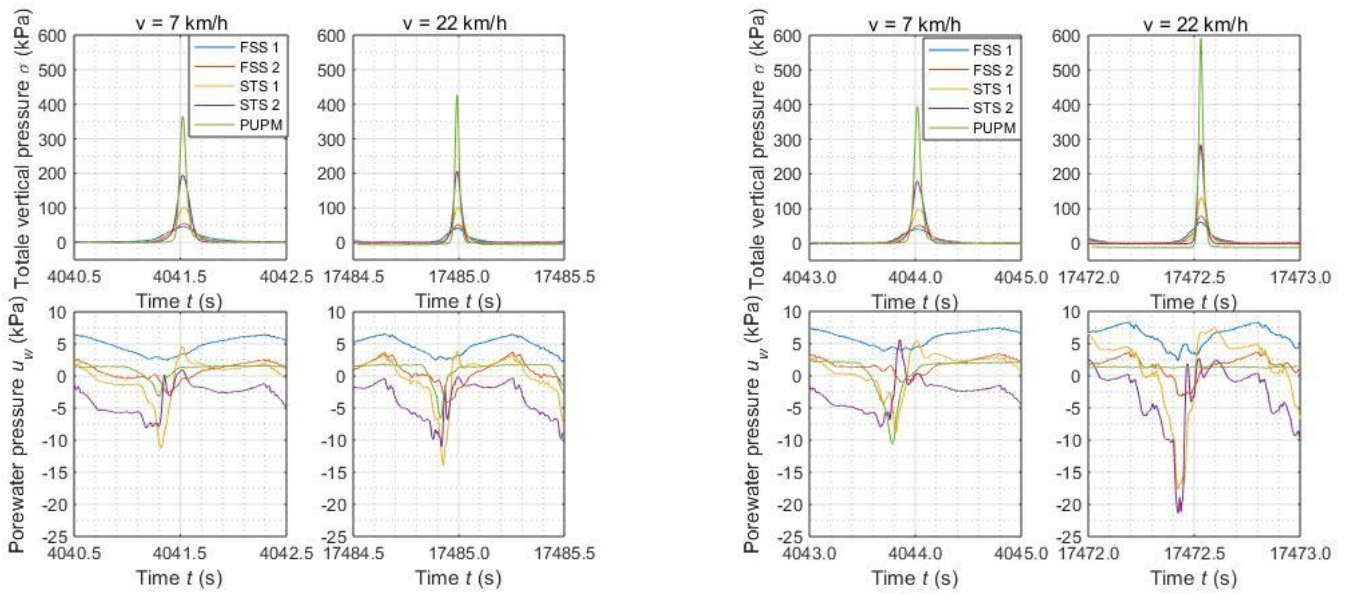
21 5 Results and Analysis

22 5.1 Multi-physical monitoring of pervious pavement

23 Figure 6 shows the responses in terms of total vertical stresses and pore-water pressures for
 24 the load cases (low saturation state and high saturation state, respectively), considering a tire

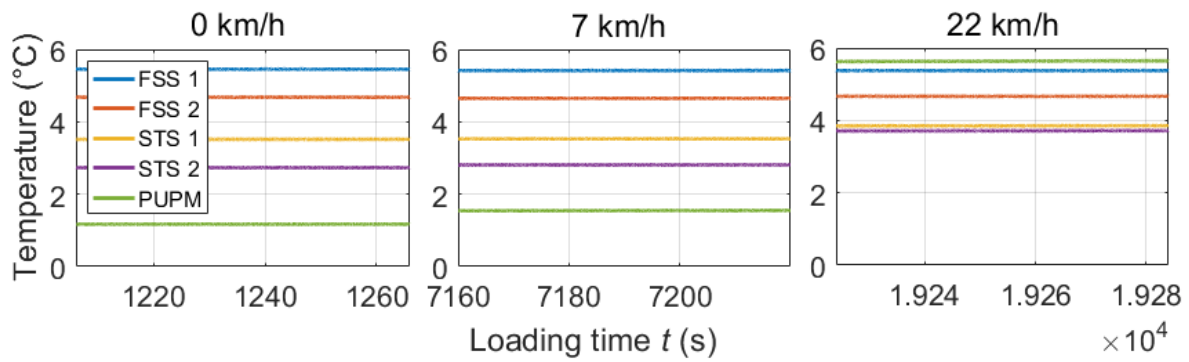
1 speed of 7 and 22 km/h. Contrary to the observations in previous truck passages experiments
2 (Lu, G. et al. 2020b), no pumping effect was observed in the lower layers as a result of accu-
3 mulated pore-pressures. However, the magnitudes of the variation in vertical stress and pore-
4 pressure were considerably higher, especially for the UGB layers. As can be seen in Figure 6,
5 both vertical stress and pore water pressures increase as the saturation increases. When com-
6 paring the low saturation state and the high saturation state, it was found that large discrepan-
7 cies were observed: more than 50kPa and 10kPa for the vertical stress and the pore water pres-
8 sure of UGB layer, respectively.

9 Due to the high porosity and permeability of the PUPM layer, the pore water pressure in the
10 surface layer was nearly zero. When comparing to the high stiffness of PUPM, the impact of
11 pore-water pressure can be neglected (Lu, G. et al. 2019a). However, high stresses and defor-
12 mation in the unbound base layers may lead to the formation of growing cavities between the
13 bound and unbound layers below the loading area, leading to failure. The causes for the signif-
14 icant deformations may be attributed to the damage mechanisms which are accelerated by the
15 presence of water and the high loads transferred to the unbound layers through the rather thin
16 surface layer. Hence, the detailed investigation of the behavior of unbound granular material in
17 terms of hydro-mechanical interaction is crucial to the long-term performance and design of
18 pervious pavement structures. Based on different loading speeds and pavement saturations, the
19 development of temperature within the pavement was also recorded (Figure 6, c & d)

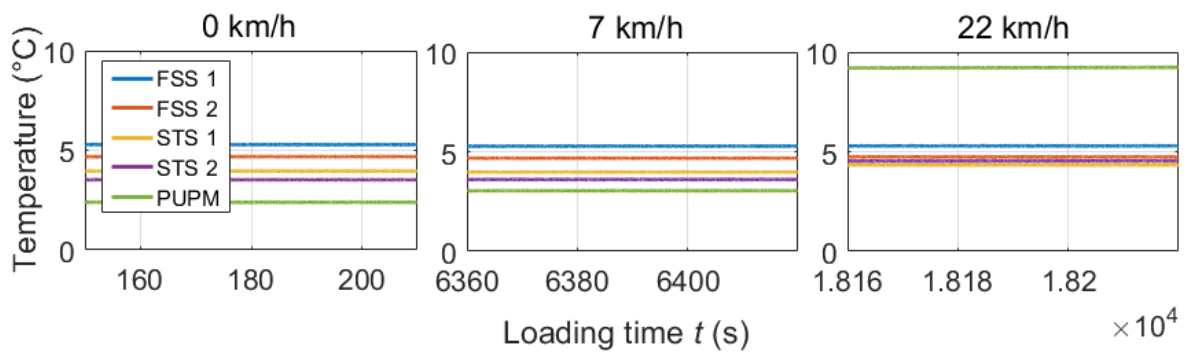


(a)

(b)



(c)



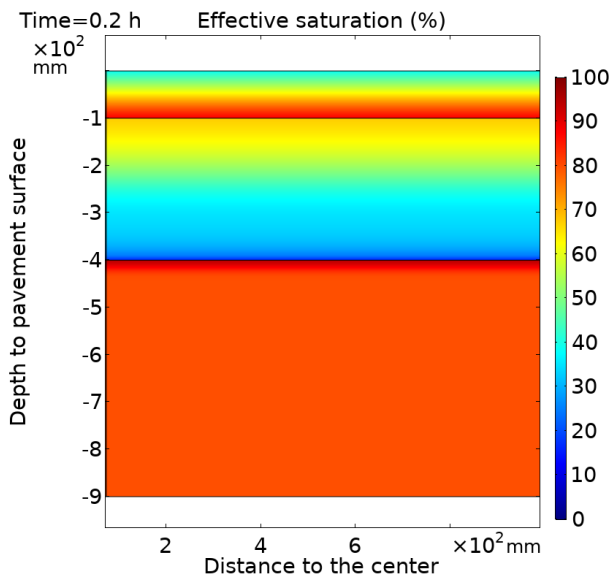
(d)

- 1 Figure 6 Field measurement of vertical stress and pore-water pressure subjected to one load-
- 2 ing process of the APT test: (a) Dry state (Low saturated state); (b) Saturated state (High satu-
- 3 rated state); (c) pavement temperature of the dry state; (d) pavement temperature of the satu-
- 4 rated states (The air temperature of the day was approximate 2-6 $^{\circ}\text{C}$).

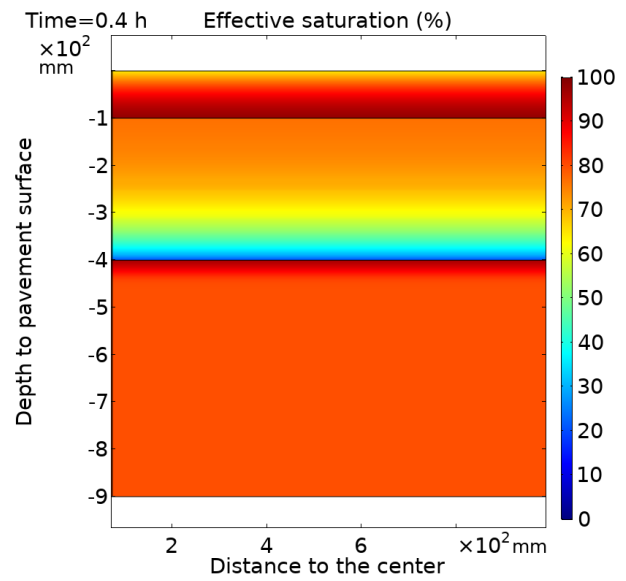
5.2 The unsaturated flow modeling for pervious pavement material

To achieve the designed permeability, the maximum design rainfall event of 270 l/ (s·ha) (l=liter, s=second and ha=hectare) was determined based on the previous laboratory column irrigation test (Lu, G. et al. 2020b). The rainfall of 0.7h duration was applied to the pervious surface. Figure 7 presents the effective saturation distribution in the entire FPP structure in terms of different watering durations. Due to the permeability levels of different layers ($H_{PUPM} > H_{UGB} > H_{subgrade}$) in the test track, rain water quickly saturated the PUPM layer from the bottom at the beginning of a rainfall event. After 0.4h of irrigation, the PUPM layer was nearly fully saturated with an average effective saturation of 92.80% (Figure 7, a). In the UGB layer, saturation developed from top to bottom. In the beginning of the irrigation event, less water infiltrated into UGB layer, with most of rainwater accumulating in the interface between the PUPM and the UGB. However, the infiltration rate increased after the PUPM layer was saturated. In this case, the water infiltrating into the UGB layer is not only driven by gravity but also by the hydraulic head in the PUPM layer (Figure 7, b). After 0.7h of irrigation, both PUPM and UGB layers are nearly fully saturated, where water cannot infiltrate into the subsoil due to the very low hydraulic conductivity in a well-compacted subsoil layer. Once this stage is reached, additional rainwater will not directly enter the pavement structure but only accumulate on the road surface (Figure 7, c). The process of saturation in the subgrade is very slow. Around one hour after the rainfall event is completed, this process exhibits significant changes. After about 2.3 hours, the irrigation is stopped and only a significant downward movement of rainwater in the pavement structure can be observed (Figure 7, d). This phenomenon corresponds to the observations during the experimental process and was selected for the further simulation of the hydro-mechanical interaction.

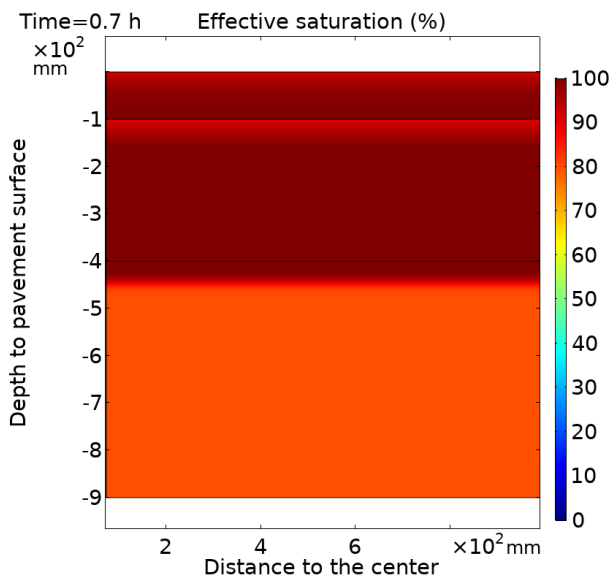
The results of the simulated water content distribution are very close to the state of the water distribution in the actual experiment, as can be seen from the measured volumetric water content in Figure 8.



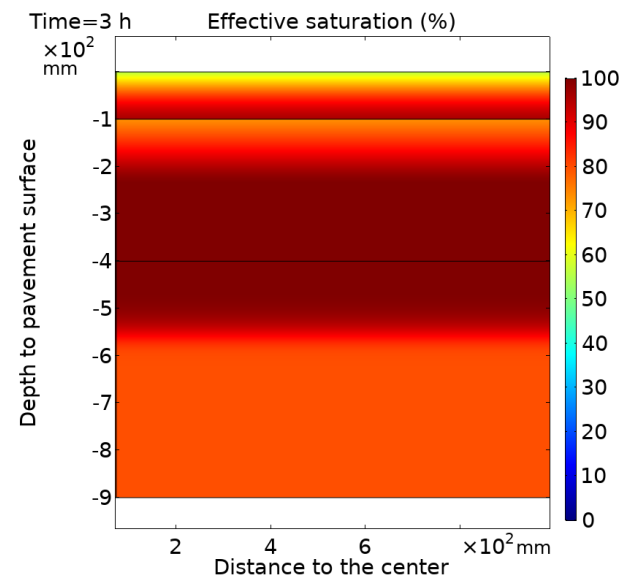
(a)



(b)



(c)



(d)

- 1 Figure 7 The effective saturation distribution based on unsaturated flow modeling: (a) The
- 2 effective saturation distribution after 0.2-hour rainfall; (b) The effective saturation distribution
- 3 after 0.4-hour rainfall; (c) The effective saturation distribution after 0.7-hour rainfall; (d) The
- 4 effective saturation distribution after 3- hour rainfall (0.7h rainfall event +2.3h rest).

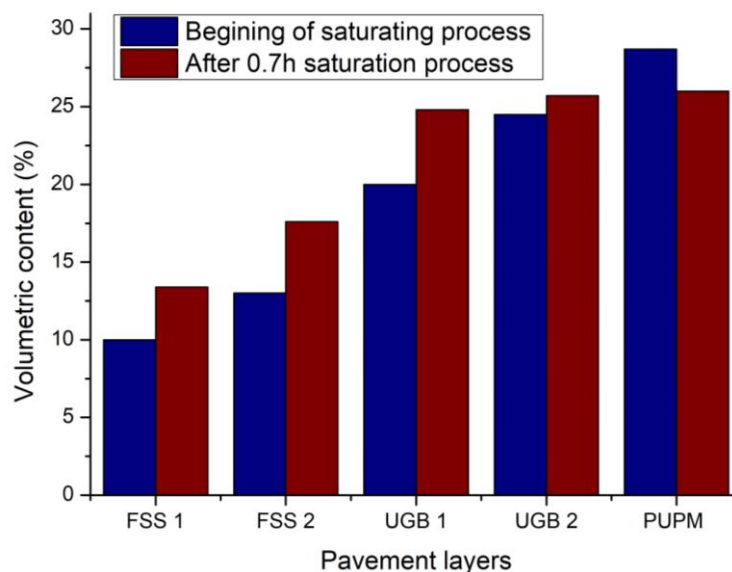


Figure 8 The measured volumetric content

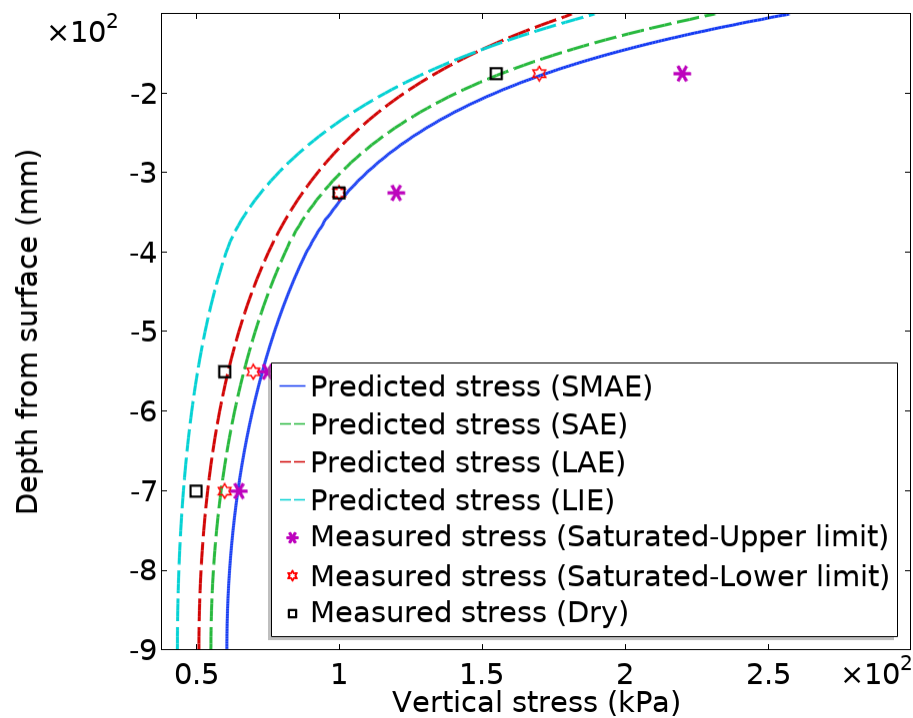
5.3 The validation and pavement response analysis based on hydro-mechanical models

The validation of the analytical model

To validate the established FEMs, the vertical stress underneath the wheel path in the base course was compared for different UGB models, including the SMAE model, the SAE model, the LAE model and the LIE model; these were compared to the field measurements from the embedded total pressure sensors. It should be noted that under fully saturated conditions the measured vertical stress was given in a range due to the large fluctuation stated in the previous section; under dry conditions, the vertical stress exhibited less variation and was given as an average value.

As can be seen in Figure 9, the results of all models follow a similar pattern. The vertical stresses are similar in magnitude and decrease with depth. In general, the vertical stresses measured in the saturated state were higher than the stresses measured in dry conditions. It is because the total vertical pressure measured is the sum of water pressure and effective pressure, and the water pressure in the saturated state is higher than that in the dry state. For the saturated state, only the vertical stresses predicted by SMAE model were in the range of the measured value. For the dry state, only the prediction made by SAE model is consistent with the measured

1 vertical stress, while the other models significantly underestimated the actual stress state by
 2 neglecting the effect of non-linear and anisotropic characteristics. It should be noted that in the
 3 subgrade, the measured vertical stresses were lower than the predictions made by the SAME
 4 and SAE model, it may be caused by the soil arching effect over the pressure sensors during
 5 the construction process, which has also been observed in the previous research (Gu, F. et al.
 6 2018). Nevertheless, the results showed that the proposed SMAE model and the weak form
 7 equation-based FEM simulation can accurately describe the response of real scale permeable
 8 pavement structures subjected to accelerated loading under different degrees of saturation.



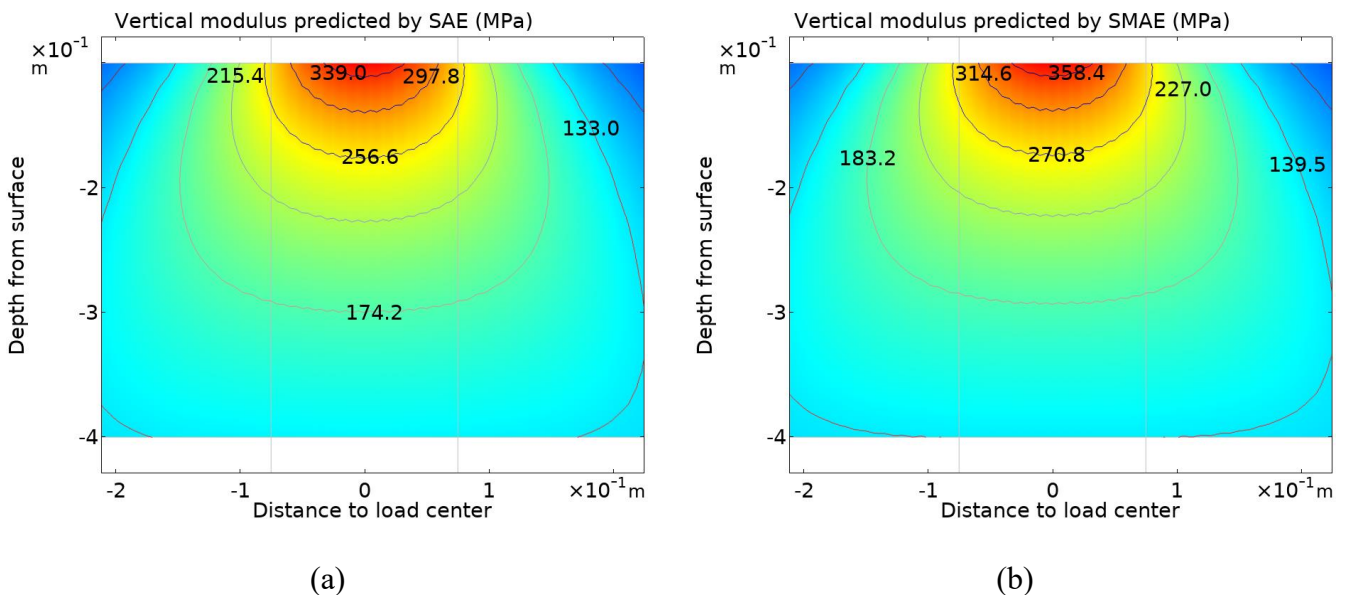
9

10 Figure 9 Validation of different UGB models based on vertical stress measured under the
 11 PUPM layer by the total pressure sensors

12 *Analysis of the resilient modulus distribution and the pavement response under different* 13 *saturations*

14 Figure 10 shows the resilient modulus distribution in the UGB layer by taking into account
 15 both the stress states and the pore-water pressures. The resilient modulus is not uniformly dis-
 16 tributed in UGB layer when considering stress-dependency. The high resilient modulus values
 17 are observed near the interfacial edges between the PUPM layer and the UGB layer. The first
 18 principal stress in these areas is very high and the octahedral shear stress is relatively small.

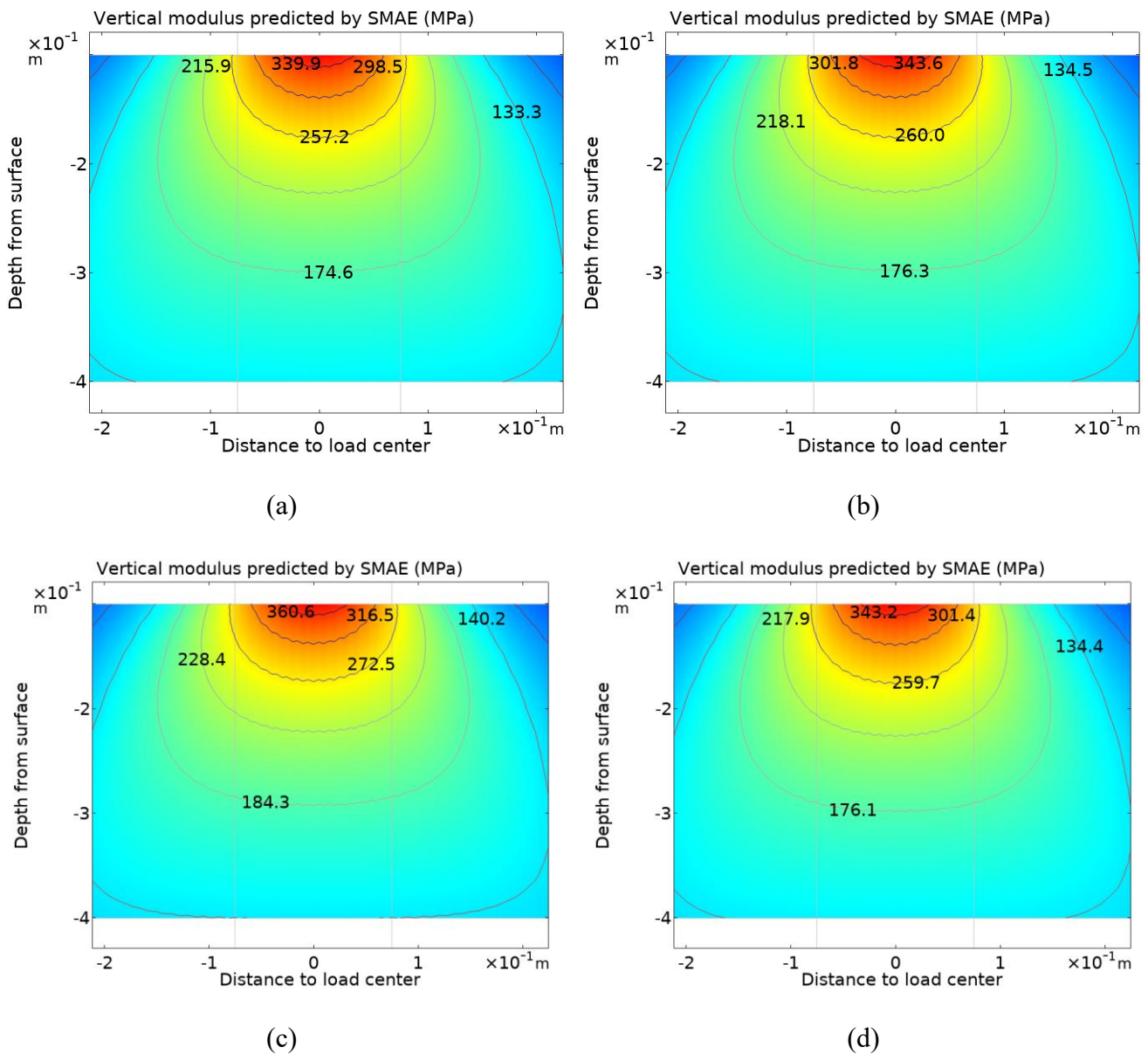
1 Many research studies have shown that increasing the first principal stress (confinement effect)
 2 and decreasing the octahedral shear stress (shearing effect) lead to a higher material stiffness.
 3 Furthermore, it is also found out that the resilient modulus of the UGB layer based on the
 4 SMAE model (Figure 10, b, high saturated state) is generally higher than that based on the SAE
 5 model (Figure 10, a, dry state). This phenomenon can be attributed to the fact that matric suc-
 6 tion (pore water pressures) acts as a confinement stress increasing the resilient modulus in par-
 7 tially saturated porous material (Gu, F. et al. 2014, Darkshanamurthy, V. et al. 1984). Therefore,
 8 both SAE and SMAE models can be used to describe the influence of the stress level on the
 9 resilient modulus of the UGB layer under dry and partially saturated states respectively.



10 Figure 10 Resilient modulus distribution in UGB layer based on: a) the SAE model (Dry
 11 conditions) and b) the SMAE model (92% saturated).

12 In order to further study the variation of stress states in the FPP structure during a rainfall
 13 event, the resilient modulus of the UGB layer was calculated with the SMAE model for differ-
 14 ent saturation states (Figure 11). As can be seen from the results, the resilient modulus of the
 15 UGB layer changes due to the water distribution. With the increase of rainfall time, the satura-
 16 tion level of the UGB increases; the resilient modulus also increases. Under fully saturated
 17 conditions, the resilient modulus reaches a maximum of 384.5 MPa at the top of the UGB
 18 layer (Figure 11c). After the rainfall event, as the water distribution percolates into the subsoil,

1 the resilient modulus of the UGB layer experiences a decrease (Figure 11, d).

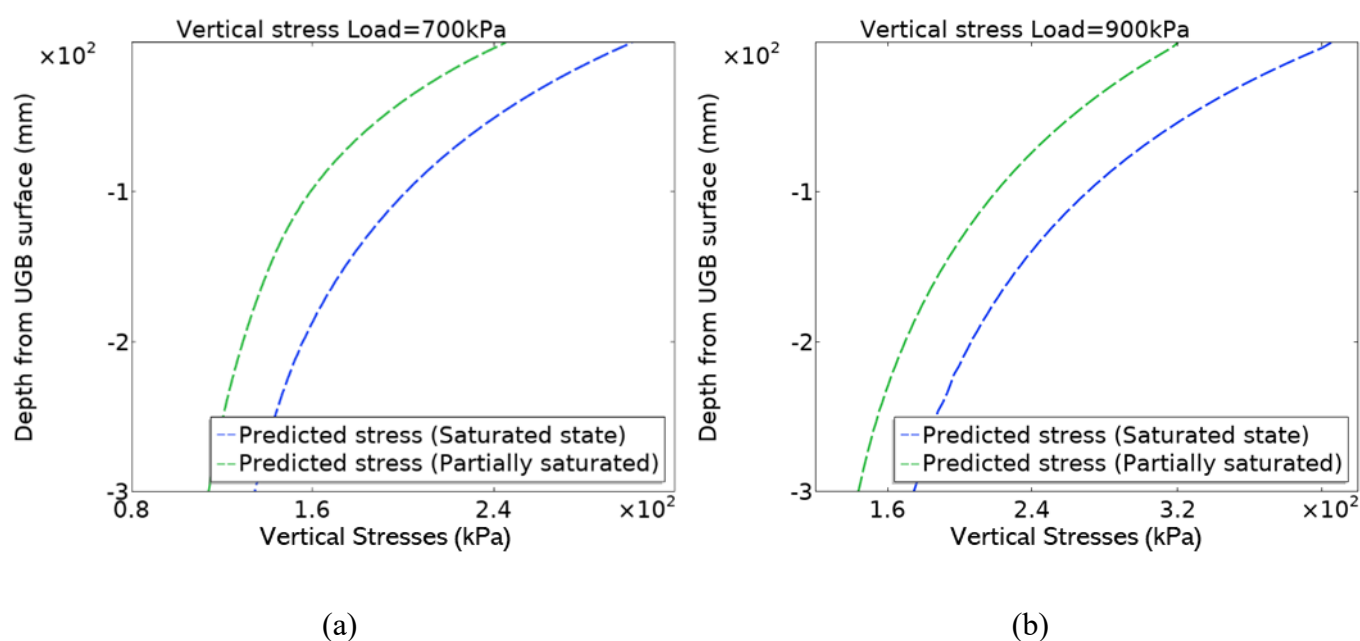


2 Figure 11 The resilient modulus of the UGB layer subjected to different saturation states in
 3 different rainfall stages: (a) 0.2h rainfall event with average effective saturation of 46% in the
 4 UGB layer; (b) 0.4h rainfall event with average effective saturation of 58% in the UGB layer;
 5 (c) 0.7h rainfall event with average effective saturation of 96% in the UGB layer; and (d)
 6 5h rainfall event (0.7h rainfall + 4.3h rest), with average effective saturation of 55% in the UGB
 7 layer

8 5.4 Prediction of the stress state in UGB subjected to heavy vehicle loads

9 In order to facilitate the wide application of permeable pavements, the pavement needs to be
 10 more stable and able to withstand heavier loads, especially in fully saturated conditions. To
 11 verify the response of the original permeable pavement structure under heavy vehicle loads, a

1 uniform load of 700 kPa and 900 kPa are applied to the pavement structure through the pro-
 2 posed FEM models. Since there is no absolutely dry state in the real application, a low satura-
 3 tion state was also considered to be compared with the fully saturated state. Figure 12 shows
 4 that as the applied stress increases, the stress level of the whole UGB layer is greatly increased.
 5 The vertical stress at the top of UGB layer even reached at 300MPa and 400MPa under surface
 6 loading of 700kPa and 900kPa respectively in fully saturated state. In addition, water distribu-
 7 tion also has a larger influence on the stress level when higher loads are applied. However,
 8 unbound granular materials are unable to sustain such high vertical stresses. This indicates that
 9 it is necessary to modify the design of current permeable pavement structure, to ensure the
 10 stable stress state in the UGB layer.

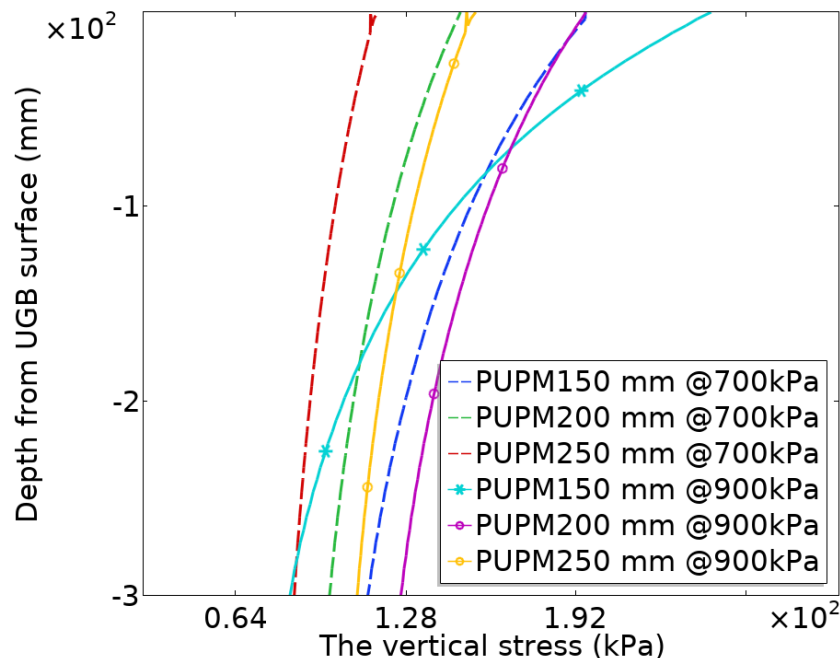


11 Figure 12 The simulation of stress state in UGB layer subjected to heavy vehicle loads of
 12 700kPa and 900kPa

13 To ensure that the hydraulic conductivity of fully permeable pavements is not diminished,
 14 optimized design can be only aimed to increase the modulus of the structural layers of the
 15 pavement and by increasing the thickness of the pervious surface. The modulus of the PUPM
 16 has already reached a very high level for porous materials; and the modulus of the base layer
 17 is difficult to increase by construction processes without adding other materials (Geogrid etc).

1 The most simple and effective approach to improve the design is to increase the thickness of
 2 the surface layer and investigate the critical design thickness of the PUPM layer for fully per-
 3 meable pavement subjected to different load levels.

4 Based on the simulation results in Figure 13, the vertical stress of the UGB is reduced sig-
 5 nificantly compared to the results in Figure 12 by increasing the thickness of the surface layer.
 6 Therefore, to ensure reasonable and stable vertical stress levels in the UGB layer for engineer-
 7 ing applications, the minimum thickness of PUPM layer could be designed to be 15 and 20 cm
 8 when the applied design load is 700 kPa and 900 kPa respectively.



9

10 Figure 13 The simulation of vertical stress in the UGB layer in the permeable pavement
 11 under fully saturated conditions based on different PUPM surface thickness and load levels
 12 with the SAME model

13 6 Conclusions

14 In the present research, the responses of permeable pavement structures to heavy vehicle
 15 loads under different saturations were determined based on the in-situ measurements as well
 16 as numerical simulations. Based on the developed SAME model, the distribution of water in
 17 the whole pavement structure was evaluated; also, the influence of the water content on the
 18 resilient modulus distribution within the UGB layer was analyzed. By estimating the stress

1 state of the UGB layer subjected to different loading conditions, the sensitivity analysis was
2 also proposed.

3 The main results can be summarized as follows:

- 4 • Based on the full-scale APT tests on a test track under different saturations, the stress
5 state of the pavement was observed to vary with the content and distribution of water
6 within the pavement structure. To be precise, the higher the water content or satura-
7 tion of each layer, the higher the stress level was observed to be. Additionally, the
8 pore water pressure also increases with the saturation level. This may cause moisture
9 damage to the structural layer as well as erosion.
- 10 • Based on Richard's equation, the unsaturated flow in the fully permeable pavement
11 can be simulated and used to evaluate the distribution of water in the pavement in
12 terms of watering time. Due to the difference in permeability of each layer, the PUPM
13 layer is saturated first at the beginning of a rainfall event, followed by the UGB layer.
14 When the PUPM and the UGB layers are both saturated, the rainwater will not infil-
15 trate into the underlying layers because the base soil has a relatively low permeabil-
16 ity.
- 17 • Among the proposed constitutive models, the results of the SAME simulation are
18 most consistent with the experimental stress levels under partially saturated condi-
19 tions, while the SAE approach presents consistent results under dry conditions. If the
20 models only consider linear elasticity, the predicted stress level is much smaller than
21 the measured one. The results confirmed the importance of nonlinear anisotropy in
22 simulating the UGB and to improve the accuracy of simulation models. Pore-water
23 pressure can be treated as confinement stress for the resilient modulus of the UGB.
24 As the saturation of each layer changes, the resilient modulus of the UGB layer also
25 changes and reaches its maximum when the layer is fully saturated.
- 26 • Based on the SMAE simulation of the stress distribution of the FPP under heavy

1 loading conditions, it is found that the influence of water on the stress state increases
2 as the applied load is increased. This insight can be used to optimize the design of
3 the FPP.

4 Overall, in the present research, an effective evaluation and prediction method is proposed
5 for a permeable pavement structure based on the novel PUPM. The impact of shear forces
6 induced by the wheel loading was not considered in this study. In permeable pavement struc-
7 tures, shear forces can lead to an expansive phenomenon that creates fluid suction into the
8 granular skeleton, followed by an excess of pore-pressure during the skeleton's elastic recov-
9 ery. Dilation and erosion may occur in dense granular soils subjected to high shear forces, with
10 void ratios below a critical value. In this case, further research on the structural material in FPP
11 based on plastic deformation theory is necessary.

12 **References**

- 13 1. Adu-Osei, A., Little, D.N. and Lytton, R.L., 2001. Cross-anisotropic charac-
14 terization of unbound granular materials. *Transportation Research Record*,
15 1757(1), pp.82-91.
- 16 2. Alobaidi, I. and Hoare, D.J., 1996. The development of pore water pressure at
17 the subgrade-subbase interface of a highway pavement and its effect on pump-
18 ing of fines. *Geotextiles and geomembranes*, 14(2), pp.111-135.
- 19 3. ASTM D6836-16, Standard Test Methods for Determination of the Soil Water
20 Characteristic Curve for Desorption Using Hanging Column, Pressure Extrac-
21 tor, Chilled Mirror Hygrometer, or Centrifuge, 2016. doi: 10.1520/D6836-16,
22 ASTM International, West Conshohocken, PA
- 23 4. Applied Research Associates (ARA). (2004). "Guide for mechanistic-empiri-
24 cal design of new and rehabilitated pavement structures." NCHRP 1-37A Fi-
25 nal Rep., Transportation Research Board, Washington, DC.
- 26 5. Bishop, A.W., 1954. The use of pore-pressure coefficients in practice. *Ge-
27 otechnique*, 4(4), pp.148-152.
- 28 6. Brattebo, B.O. and Booth, D.B., 2003. Long-term stormwater quantity and
29 quality performance of permeable pavement systems. *Water research*, 37(18),
30 pp.4369-4376.
- 31 7. Brooks, R. and Corey, T., 1964. HYDRAUC properties of porous media.
32 *Hydrology Papers*, Colorado State University, 24, p.37.

- 1 8. Cao, R., Leng, Z., Hsu, S. C., & Hung, W. T. (2020). Modelling of the pave-
2 ment acoustic longevity in Hong Kong through machine learning techniques.
3 *Transportation Research Part D: Transport and Environment*, 83, 102366.
- 4 9. Carrier III, W.D., 2003. Goodbye, hazen; hello, kozeny-carman. *Journal of*
5 *geotechnical and geoenvironmental engineering*, 129(11), pp.1054-1056.
- 6 10. Celia, M.A., Bouloutas, E.T. and Zarba, R.L., 1990. A general mass-conserva-
7 tive numerical solution for the unsaturated flow equation. *Water resources re-*
8 *search*, 26(7), pp.1483-1496.
- 9 11. Darkshanamurthy, V., Fredlund, D.G. and Rahardjo, H., 1984. Coupled three-
10 dimensional consolidation theory of unsaturated porous media. In *Fifth Inter-*
11 *national Conference on Expansive Soils 1984: Preprints of Papers* (p. 99). In-
12 *stitution of Engineers, Australia.*
- 13 12. Ding, Y., & Wang, H. (2019). FEM-BEM analysis of tyre-pavement noise on
14 porous asphalt surfaces with different textures. *International Journal of Pave-*
15 *ment Engineering*, 20(9), 1090-1097.
- 16 13. Fredlund, D.G. and Rahardjo, H., 1993. *Soil mechanics for unsaturated soils.*
17 *John Wiley & Sons.*
- 18 14. Fredlund, D.G. and Xing, A., 1994. Equations for the soil-water characteristic
19 curve. *Canadian geotechnical journal*, 31(4), pp.521-532.
- 20 15. Gray, W.G. and Hassanizadeh, S.M., 1991. Unsaturated flow theory including
21 interfacial phenomena. *Water Resources Research*, 27(8), pp.1855-1863.
- 22 16. Gu, F., Luo, X., Zhang, Y., Chen, Y., Luo, R. and Lytton, R.L., 2018. Predic-
23 tion of geogrid-reinforced flexible pavement performance using artificial neu-
24 ral network approach. *Road Materials and Pavement Design*, 19(5), pp.1147-
25 1163.
- 26 17. Gu, F., Sahin, H., Luo, X., Luo, R. and Lytton, R.L., 2014. Estimation of re-
27 siliant modulus of unbound aggregates using performance-related base course
28 properties. *Journal of Materials in Civil Engineering*, 27(6), p.04014188.
- 29 18. Hall, C., 1977. Water movement in porous building materials—I. Unsaturated
30 flow theory and its applications. *Building and Environment*, 12(2), pp.117-
31 125.
- 32 19. Kettil, P., Engström, G. and Wiberg, N.E., 2005. Coupled hydro-mechanical
33 wave propagation in road structures. *Computers & structures*, 83(21-22),
34 pp.1719-1729.
- 35 20. Khalili, N., Geiser, F. and Blight, G.E., 2004. Effective stress in unsaturated
36 soils: Review with new evidence. *International journal of Geomechanics*, 4(2),
37 pp.115-126.
- 38 21. Khalili, N., Russell, A. and Khoshghalb, A. eds., 2014. *Unsaturated soils: re-*
39 *search & applications.* Crc Press.
- 40 22. Li, H., Jones, D. and Harvey, J., 2012. Development of Mechanistic–Empiri-
41 cal Design Procedure for Fully Permeable Pavement under Heavy Traffic.
42 *Transportation Research Record*, 2305(1), pp.83-94.

- 1 23. Liu, P., Otto, F., Wang, D., Oeser, M. and Balck, H., 2017. Measurement and
2 evaluation on deterioration of asphalt pavements by geophones. *Measurement*,
3 109, pp.223-232.
- 4 24. Liu, Z. and Yu, X., 2014. Coupled thermo-hydraulic modelling of pavement
5 under frost. *International Journal of Pavement Engineering*, 15(5), pp.427-
6 437.
- 7 25. Loret, B. and Khalili, N., 2002. An effective stress elastic–plastic model for
8 unsaturated porous media. *Mechanics of Materials*, 34(2), pp.97-116.
- 9 26. Lu, G., Renken, L., Li, T., Wang, D., Li, H. and Oeser, M., 2019a. Experi-
10 mental study on the polyurethane-bound pervious mixtures in the application
11 of permeable pavements. *Construction and Building Materials*, 202, pp.838-
12 850.
- 13 27. Lu, G., Liu, P., Wang, Y., Faßbender, S., Wang, D. and Oeser, M., 2019b.
14 Development of a sustainable pervious pavement material using recycled ce-
15 ramic aggregate and bio-based polyurethane binder. *Journal of Cleaner Pro-
16 duction*, 220, pp.1052-1060.
- 17 28. Lu, G., Wang, Z., Liu, P., Wang, D. and Oeser, M., 2020a. Investigation of the
18 Hydraulic Properties of Pervious Pavement Mixtures: Characterization of
19 Darcy and Non-Darcy Flow Based on Pore Microstructures. *Journal of Trans-
20 portation Engineering, Part B: Pavements*, 146(2), p.04020012.
- 21 29. Lu, G., Törzs, T., Liu, P., Zhang, Z., Wang, D., Oeser, M. and Grabe, J., 2020b.
22 Dynamic Response of Fully Permeable Pavements: Development of Pore
23 Pressures under Different Modes of Loading. *Journal of Materials in Civil En-
24 gineering*, 32(7), p.04020160.
- 25 30. Lu, G., Wang, H., Törzs, T., Liu, P., Zhang, Y., Wang, D., Oeser, M. and
26 Grabe, J., 2020c. In-situ and numerical investigation on the dynamic response
27 of unbounded granular material in permeable pavement. *Transportation Ge-
28 otechnics*, p.100396.
- 29 31. Luo, X., Li, H., Deng, Y. and Zhang, Y., 2020. Energy-Based Kinetics Ap-
30 proach for Coupled Viscoplasticity and Viscoplasticity of Asphalt Mixtures.
31 *Journal of Engineering Mechanics*, 146(9), p.04020100.
- 32 32. Mo, L., Hurman, M., Wu, S. and Molenaar, A.A.A., 2009. Ravelling inves-
33 tigation of porous asphalt concrete based on fatigue characteristics of bitu-
34 men–stone adhesion and mortar. *Materials & Design*, 30(1), pp.170-179.
- 35 33. Mualem, Y., 1977. Extension of the similarity hypothesis used for modeling
36 the soil water characteristics. *Water Resources Research*, 13(4), pp.773-780.
- 37 34. Oeser, M., Hovagimian, P. and Kabitzke, U., 2012. Hydraulic and mechanical
38 properties of porous cement-stabilised materials for base courses of PICPs.
39 *International Journal of Pavement Engineering*, 13(1), pp.68-79.
- 40 35. Renken, L., Oeser, M., Milatz, M. and Grabe, J., 2015, October. Measurement
41 of hydraulic properties of unsaturated permeable polyurethane bound asphalt
42 materials. In *Unsaturated Soil Mechanics-from Theory to Practice: Proceed-
43 ings of the 6th Asia Pacific Conference on Unsaturated Soils (Guilin, China,
44 23-26 October 2015)* (p. 407). CRC Press.

- 1 36. Scholz, M. and Grabowiecki, P., 2007. Review of permeable pavement sys-
2 tems. *Building and Environment*, 42(11), pp.3830-3836.
- 3 37. Sun, W., Lu, G., Ye, C., Chen, S., Hou, Y., Wang, D., Wang, L. and Oeser,
4 M., 2018. The state of the art: application of green technology in sustainable
5 pavement. *Advances in Materials Science and Engineering*, 2018.
- 6 38. Tutumluer, E. and Thompson, M.R., 1997. Anisotropic modeling of granular
7 bases in flexible pavements. *Transportation research record*, 1577(1), pp.18-
8 26.
- 9 39. Törzs, T., Lu, G., Monteiro, A.O., Wang, D., Grabe, J. and Oeser, M., 2019.
10 Hydraulic properties of polyurethane-bound permeable pavement materials
11 considering unsaturated flow. *Construction and Building Materials*, 212,
12 pp.422-430.
- 13 40. Uzan, J., 1985. Characterization of granular material. *Transportation research*
14 *record*, 1022(1), pp.52-59.
- 15 41. Valvatne, P.H. and Blunt, M.J., 2004. Predictive pore-scale modeling of two-
16 phase flow in mixed wet media. *Water resources research*, 40(7).
- 17 42. Van Genuchten, M.T., 1980. A closed-form equation for predicting the hy-
18 draulic conductivity of unsaturated soils 1. *Soil science society of America*
19 *journal*, 44(5), pp.892-898.
- 20 43. Wang, C.Y. and Cheng, P., 1997. Multiphase flow and heat transfer in porous
21 media. In *Advances in heat transfer* (Vol. 30, pp. 93-196). Elsevier.
- 22 44. Zhang, Y. and Leng, Z., 2017. Quantification of bituminous mortar ageing and
23 its application in ravelling evaluation of porous asphalt wearing courses. *Ma-*
24 *terials & Design*, 119, pp.1-11.
- 25 45. Zhang, J., Li, J., Yao, Y., Zheng, J. and Gu, F., 2018. Geometric anisotropy
26 modeling and shear behavior evaluation of graded crushed rocks. *Construction*
27 *and Building Materials*, 183, pp.346-355.
- 28 46. Zhang, Y., Birgisson, B. and Lytton, R.L., 2015. Weak form equation-based
29 finite-element modeling of viscoelastic asphalt mixtures. *Journal of Materials*
30 *in Civil Engineering*, 28(2), p.04015115.
- 31 47. Zhang, Y., Gu, F., Birgisson, B. and Lytton, R.L., 2017. Viscoelasticplastic-
32 Fracture Modeling of Asphalt Mixtures Under Monotonic and Repeated
33 Loads. *Transportation Research Record*, 2631(1), pp.20-29.
- 34 48. Zhang, Y., Gu, F., Luo, X., Birgisson, B. and Lytton, R.L., 2018. Modeling
35 Stress-Dependent Anisotropic Elastoplastic Unbound Granular Base in Flexi-
36 ble Pavements. *Transportation Research Record*, p.0361198118758318.
- 37 49. Zhang, Y., Luo, R. and Lytton, R.L., 2011. Anisotropic viscoelastic properties
38 of undamaged asphalt mixtures. *Journal of Transportation Engineering*,
39 138(1), pp.75-89.